Figure S1, Related to Figure 2. Schematic showing location of all 56 recording sites in this study (red dots).
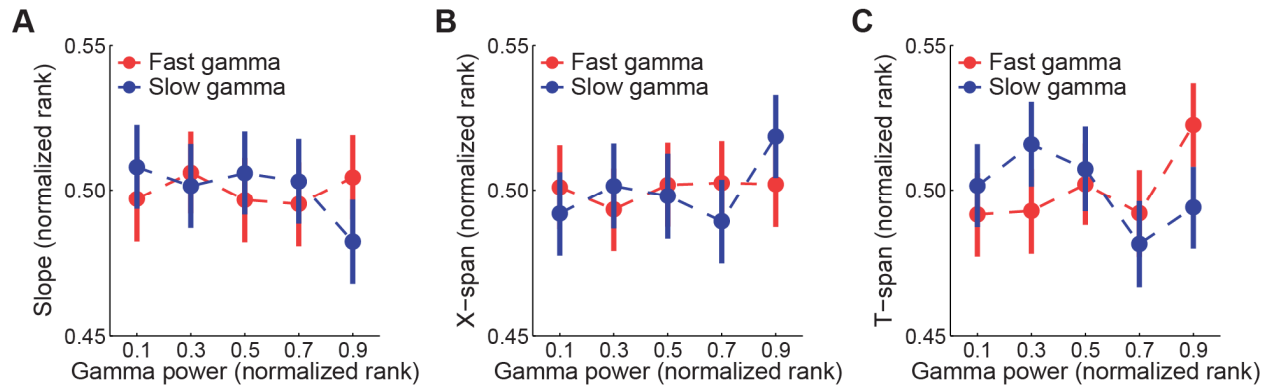
Figure S2, Related to Figure 4. No significant effects of slow and fast gamma on theta sequences with negative slopes. In all panels, gamma power measures (x-axes) were ranked separately for each gamma type. Slope **(A)**, x-span **(B)**, and t-span **(C)** as a function of slow (blue) and fast (red) gamma power for significant sequences exhibiting negative slopes. There was no gamma type × gamma power interaction effect on slope (**A**, multiple regression interaction term; b = -0.02, $t(3958)$ = -0.7, p = 0.5, n = 1981 sequences), nor was there a main effect of gamma power (b = -0.008, $t(3958)$ = -0.5, p = 0.6). There was no gamma type × gamma power interaction effect on x-span (**B**, multiple regression interaction term; b = 0.01, $t(3958)$ = 0.4, p = 0.7), nor was there a main effect of gamma power (b = 0.01, $t(3, 3958)$ = 0.6, p = 0.5). No gamma power × gamma type interaction was found for t-span (**C**; multiple regression interaction term; b = -0.04, $t(3958)$ = -1.4, p = 0.2), nor was there a main effect of gamma power (b = 0.002, $t(3958)$ = 0.1, p = 0.9).
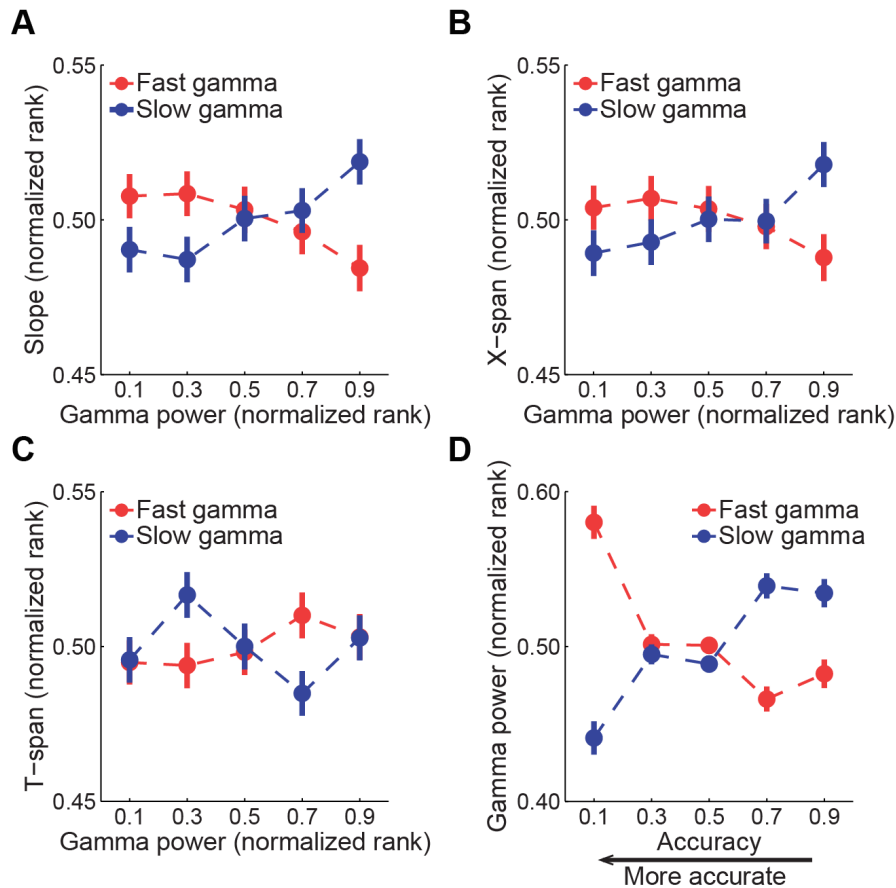
Figure S3, Related to Figure 4. **Effects of fast and slow gamma power on properties of theta sequences for different theta sequence selection criteria.** Slope (**A**), x-span (**B**), and t-span (**C**) as a function of slow (blue) and fast (red) gamma power for all significant sequences (i.e., including those with both positive and negative slopes, n = 7775 sequences). Absolute values of slopes were used to combine positive and negative slope values (A). We found a significant interaction effect of gamma power and gamma type (i.e., slow or fast) on both slope and x-span measures (multiple regression model interaction term; slope: b = 0.07, $t(15546)$ = 4.2, p < 0.001; x-span: b = 0.06, $t(15546)$ = 3.4, p = 0.001) but not t-span (b = -0.02, $t(15546)$ = -1.3, p = 0.2). Also, gamma power did not significantly affect t-spans (b = 0.002, $t(15546)$ = 0.3, p = 0.8). Slope and x-span measures increased as a function of slow gamma power (linear

regression; $b = 0.04$, $t(7773) = 3.2$, $p = 0.002$ for slope, and $b = 0.03$, $t(7773) = 2.8$, $p = 0.005$ for x-span) but decreased as a function of fast gamma power ($b = -0.03$, $t(7773) = -2.7$, $p = 0.006$ for slope, and $b = -0.02$, $t(7773) = -2.0$, $p = 0.04$ for x-span). (**D**) Slow and fast gamma power as a function of accuracy for all significant sequences (i.e., including those with both positive and negative slopes). We found that different gamma types showed different relationships to accuracy (multiple regression model interaction term; $b = 0.2$, $t(15546) = 9.8$, $p < 0.001$). High fast gamma power correlated with high accuracy ($b = -0.1$, $t(7773) = -6.6$, $p < 0.001$), and high slow gamma power correlated with low accuracy ($b = 0.1$, $t(7773) = 7.3$, $p < 0.001$).

In the main analyses, significant sequences were comprised of two groups based on two methods for determining significance of sequences (See "Theta sequence analysis and significance determination" section of Experimental Procedures). One group contained sequences with relatively steep slopes (n = 4668), and the other group contained sequences with relatively flat (i.e., near zero) slopes (n = 1173). The latter group contained a small proportion (~1/5) of all slow and fast gamma sequences (see Figure 2B). When we separated these two groups of sequences, we found a significant interaction of gamma type (i.e., slow or fast) and slope type (i.e., steep or flat) on gamma power (repeated measures ANOVA, $F(1,5839) = 7.1$, $p = 0.008$), indicating that slow and fast gamma power exhibited different relationships with different slope types. In the group of sequences with steep slopes, we found a significant interaction of gamma power and gamma type (i.e., slow or fast) on slope (multiple regression model interaction term; $b = 0.05$, $t(9332) = 2.8$, $p = 0.005$). For steep slope sequences, slow gamma power and slope were positively correlated ($b = 0.03$, $t(4666) = 2.9$, $p = 0.004$),

but fast gamma power and slope were not (b = -0.01, t(4666) = -1.1, p = 0.3). The

narrow range of slope values in the group of significant sequences with flat slopes (see

Figure 2B) hindered analysis of changes in flat slopes as a function of gamma power.

Perhaps not surprisingly then, the values of flat slopes did not change significantly with

gamma power (multiple regression model: interaction term, b = 0.01, t(2342) = 1.5, p =

0.1; effect of gamma power, b = -0.002, t(2342) = -0.5, p = 0.6).   However, for

sequences with flat slopes, fast gamma power ranks were significantly higher than slow

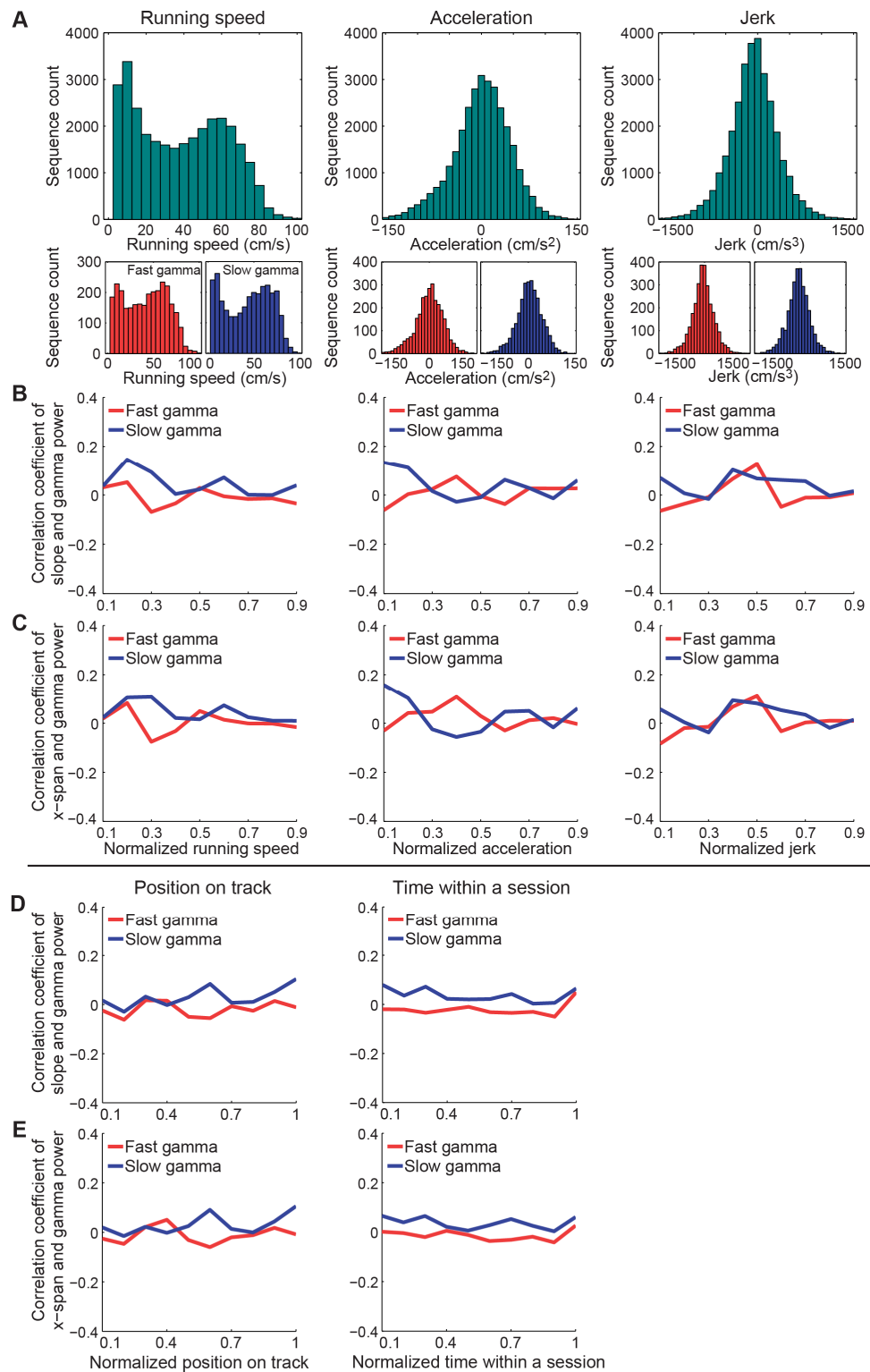gamma power ranks (paired t-test; t(1172) = 2.4, p = 0.02).

Figure S4, Related to Figure 4. Effects of behavioral state of the animal, position on the track, and time within a session on theta sequences. (A) Histogram showing

distributions of running speed, acceleration, and jerk estimates for all significant sequences (green), significant fast gamma sequences (red), and significant slow gamma sequences (blue). **(B)** Correlation between slope and fast (red) or slow (blue) gamma power as a function of normalized running speed, acceleration, and jerk. Note how the correlation between slope and gamma power does not change as a function of speed, acceleration, or jerk. **(C)** Correlation between path length (x-span) and fast (red) or slow (blue) gamma power as a function of normalized running speed, acceleration, and jerk. Note how the correlation between x-span and gamma power does not change as a function of speed, acceleration, or jerk. **(D)** Correlation between slope and fast (red) or slow (blue) gamma power as a function of normalized position on the track and time within a session. **(E)** Correlation between path length (x-span) and fast (red) or slow (blue) gamma power as a function of normalized position on the track and time within a session. Note that correlations between gamma power and slope, and between gamma power and path length, do not change systematically with track position or time within a session.
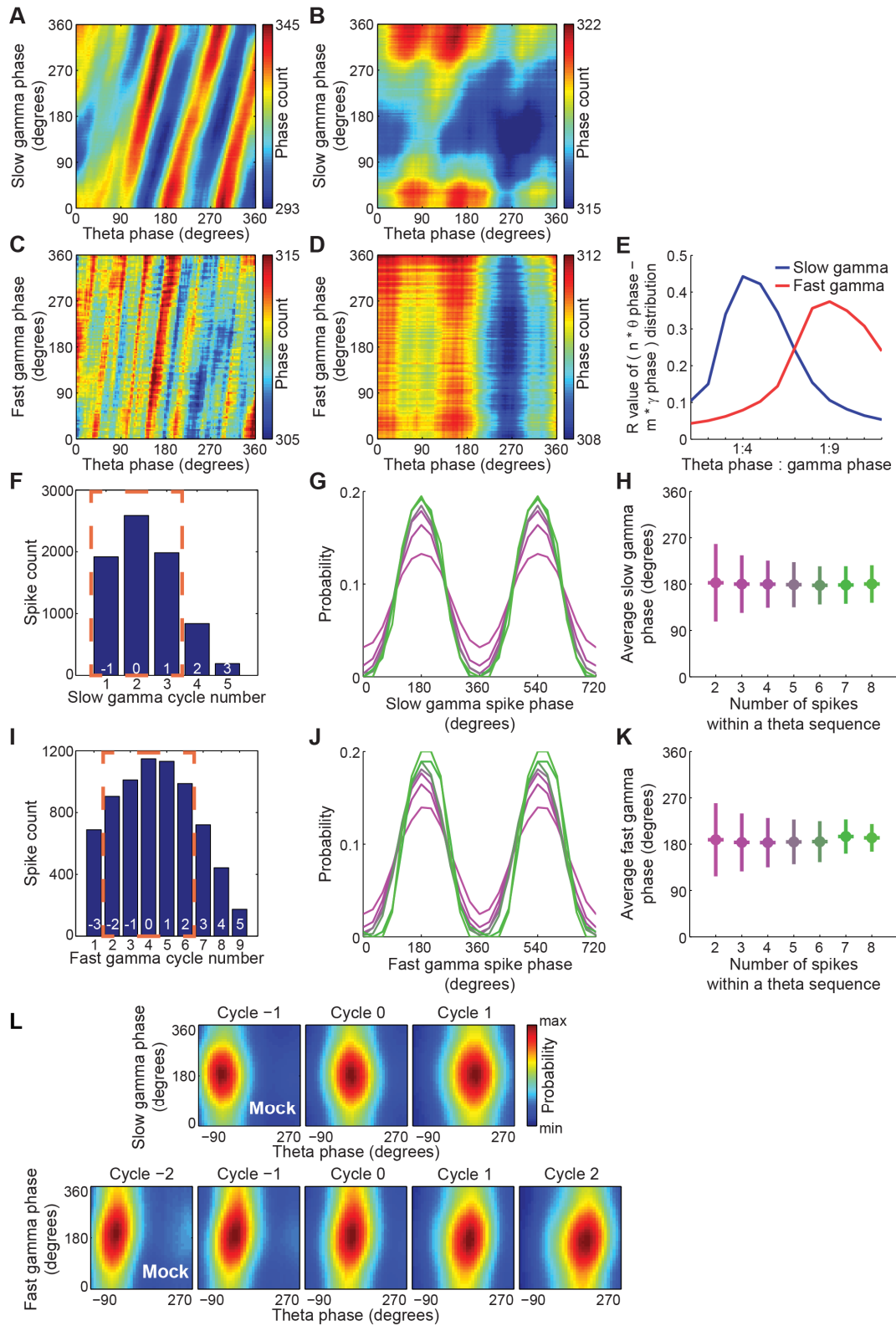
Figure S5, Related to Figure 5. Gamma phase analyses. (A-D) Theta-gamma

phase-phase plots of continuous local field potential recordings (from 56 tetrodes) **(A,**

C), and corresponding shuffled signals **(B, D)**, during slow gamma sequences **(A, B)** and fast gamma sequences **(C, D)**. Theta-gamma phase-phase coupling was apparent for both slow and fast gamma, consistent with previously published reports (Belluscio et al., 2012). Shuffling procedures were based on those published by Belluscio and colleagues (Belluscio et al., 2012; see "Phase-phase coupling" section of Supplemental Experimental Procedures). **(E)** Mean radial distance (R value) from the distribution of the differences between theta phases and gamma phases calculated for different *n:m* (number of theta cycles: number of gamma cycles) relationships. Note that peaks can be seen around 1:4 for slow gamma and 1:9 for fast gamma, consistent with previous findings (Belluscio et al., 2012). **(F, I)** Spike counts at successive slow gamma cycles **(F)** and fast gamma cycles **(I)**. Gamma cycles within theta sequences were temporally ordered, centered at cycle 0 (corresponding to the gamma cycle with maximal number of spikes). **(G-H, J-K)** Neither the preferred slow gamma phase of spiking during slow gamma sequences **(G-H)** nor the preferred fast gamma phase of spiking during fast gamma sequences **(J-K)** varied significantly according to the number of spikes within a theta sequence. Data represent angular mean ± angular deviation. **(L)** Probability distributions of gamma phases of spikes in slow gamma sequences (top) and fast gamma sequences (bottom) across mock gamma cycles that were created using an alternative method (see "Alternative method for creating mock gamma cycles" section of Supplemental Experimental Procedures). In this method, the real gamma phases were maintained within each gamma cycle, but gamma cycles were shuffled within each theta sequence. Spike times were not shuffled such that the original theta phases of spikes within each theta sequence were preserved. Slow gamma phases at spike times did

not shift significantly across mock slow gamma cycles within slow gamma sequences (top). The mean phase shift across successive slow gamma cycles for the real data was -46.0 degrees, which was significantly different than the phase shifts observed across the mock slow gamma cycles (-0.01 ± 2.9 degrees, mean ± angular deviation; 95% confidence intervals for mock data: [-4.0, 5.6] degrees, p < 0.0001). Fast gamma phases at spike times also did not shift significantly across mock fast gamma cycles within fast gamma sequences (bottom). The mean phase shift across real fast gamma cycles (-6.0 degrees) was not significantly different than the phase shifts across mock fast gamma cycles (-6.2 ± 2.9 degrees, mean ± angular deviation; 95% confidence intervals for mock data: [-9.8, -2.0] degrees, p = 1.0).
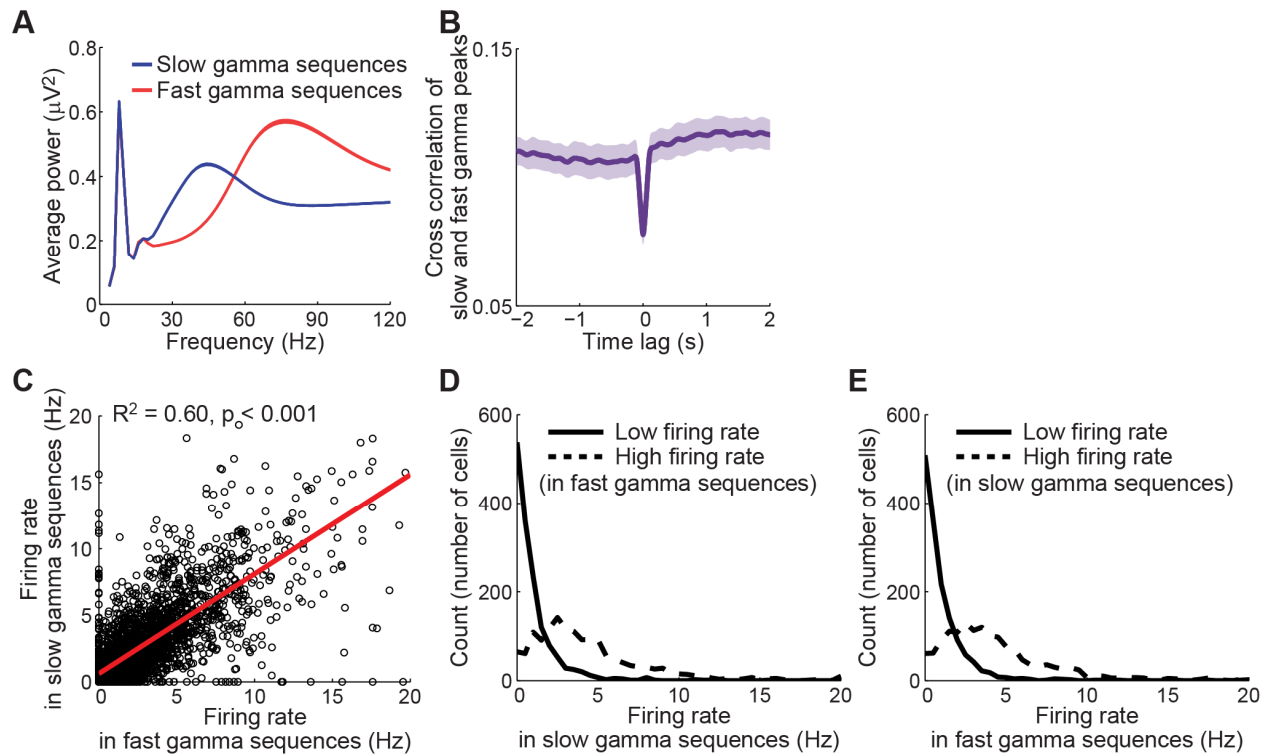
Figure S6, Related to Figure 6. Slow and fast gamma sequences did not co-occur, but individual place cells fired during both. (A) Average power spectra for fast gamma sequences (red) and slow gamma sequences (blue). **(B)** Cross-correlogram for slow gamma peaks vs. fast gamma peaks. The procedure used to detect slow and fast gamma peaks is described in the **"Cross-correlation of gamma peaks"** section of the Supplemental Experimental Procedures. Data represent mean ± SEM. **(C)** There was a significant positive correlation between the spike rate of each cell during fast gamma sequences and slow gamma sequences. Each open circle corresponds to measures from one cell. **(D-E)** Place cells were divided into low firing and high firing categories for each gamma type (see "Place cell spike rates during slow and fast gamma sequences" section of Supplemental Experimental Procedures). Place cells exhibited similar levels of activity during both gamma types. This finding is inconsistent with the hypothesis that distinct classes of place cells, corresponding to

11

'TroPyr' and 'RisPyr' cells (Senior et al., 2008), fire selectively during slow and fast gamma.

SUPPLEMENTAL EXPERIMENTAL PROCEDURES

Tetrode and recording drive preparation.

Recording drives contained 14 (6 rats) or 26 (1 rat) independently movable tetrodes constructed from 17 μm polyimide-coated platinum-iridium (90%-10%) wire (California Fine Wire). Electrode tips in tetrodes targeted toward cell body layers were platinum-plated to reduce single channel impedances to ~150-300 kΩ at 1 kHz.

Tetrode placement.

Over the course of a few weeks after drive implantation, tetrodes were slowly lowered toward their target locations. We targeted 6 of the 14 tetrodes toward the CA1 cell body layer and 6 toward the CA3 cell body layer in 4 rats (CA3 data was not used for this study), and 12 of the tetrodes toward the CA1 cell body layer in 2 rats, and 24 tetrodes toward the CA1 cell body layer in 1 rat. In all rats, 1 tetrode was targeted toward the apical dendritic layers of CA1 and was used for hippocampal depth estimation as the rest of the tetrodes were turned down. In all rats, 1 tetrode was used as a reference for differential recording. This reference tetrode was placed at the level of the corpus callosum or higher and was recorded against ground to make sure that it was placed in a quiet location. All recording locations were verified histologically after experiments were finished (see "Histology" section below). Figure S1 shows the recording locations for the 56 tetrodes that were included in this study (i.e., those that had place cells and were located in or near CA1 stratum pyramidale on the days of recording). In one rat, two tetrodes targeted toward CA1 appeared in histological sections to be on the border

of CA2-CA1. However, place cells and LFPs recorded from these tetrodes were indistinguishable from other CA1 recordings collected simultaneously. Therefore, place cells and LFPs from these tetrodes were included in this study.

Data acquisition.

Experiments began when spikes with amplitudes exceeding ~5 times the noise levels emerged around the estimated depth of CA1 (i.e., ~2 mm). Robust theta rhythms and sharp wave-ripple activity were used as on-line verification that tetrodes were in the CA1 cell body layer. Recording drives were connected to multichannel, unity gain headstages (Neuralynx, Bozeman, MT, USA). The headstage output was conducted via lightweight tether cables through a multichannel slip-ring commutator to a data acquisition system that processed the signals through individual 24 bit AD converters (Digital Lynx, Neuralynx, Bozeman, MT, USA). Unit activity was bandpass filtered from 600 to 6000 Hz. Spike waveforms above a threshold set by the experimenter (~55-75 µV) were time-stamped and recorded at 32 kHz for 1 ms. Light-emitting diodes (LEDs) on the headstages were used to track rats' movements at a 30 Hz sampling rate. Additionally, video files were collected during every recording session. LFPs (1 per tetrode) were recorded continuously in the 0.1-500 Hz band at a sampling rate of 2000 Hz. Notch filters were not used. Continuously sampled LFPs were recorded differentially against a common reference electrode placed in an electrically quiet region (see "Tetrode placement" section above). The common reference signal was duplicated using a breakout board (MDR-50 breakout board, Neuralynx, Bozeman, MT, USA) and recorded continuously against ground.

Spike sorting and cell classification.

Spike sorting was performed offline using graphical cluster-cutting software (MClust v3.5; A.D. Redish, University of Minnesota, Minneapolis). Spikes were clustered manually in two-dimensional projections of the multidimensional parameter space (consisting of waveform amplitudes, energies, and peak-to-valley ratios). Autocorrelation and cross-correlation functions were additionally used to identify single units. Putative place cells were distinguished from putative interneurons on the basis of spike width, average firing rate, and bursting properties (Fox and Ranck, 1981; Frank et al., 2001; Harris et al., 2000; Henze et al., 2000). Firing rate maps across behavioral sessions (see "Place fields" section, below) were also used to identify place cells.

Place fields.

Rats' trajectories were tracked using red and green LEDs on the headstage. Spatial firing rate distributions ("place fields") for each well-isolated putative pyramidal cell were constructed by summing the total number of spikes that occurred in a given location bin (3 cm), dividing by the amount of time that the animal spent in that bin, and smoothing with a 15 cm (5 bins) SD Gaussian centered on each bin. A total of 604 CA1 place cells were used; 351 of these cells were included in a previous study (Bieri et al., 2014).

The two track directions were analyzed separately; this was also the case for data sets containing bidirectional place cells. A minority of place cells in this study (92 out of 604 cells) were defined as bidirectional. Bidirectional place cells were defined using the following criteria from (Battaglia et al., 2004): (1) exhibited a mean firing rate

> 0.3 Hz in each direction; (2) spatial information content > 0.25 bits/spike in each direction; and (3) maximum rate overlap (R) between the rate maps in the two directions > 0.35.

Estimation of running speed.

The running speed for each position (x_n) was estimated by taking the difference between the preceding position (x_n-1) and the following position (x_n+1) and dividing by the elapsed time (2*1/position sampling frequency) (Bieri et al., 2014). The sampling frequency for position data was 30 Hz, thus allowing a temporal resolution of 1/15 seconds for running speed. Acceleration and jerk (Figure S4) were calculated as the first and second derivatives, respectively, of the running speed.

Oscillatory power estimation.

Time varying power for slow gamma (25–55 Hz), fast gamma (60–100 Hz), theta (6–10 Hz), and delta (2–4 Hz) were computed, using a wavelet transform method described previously (Tallon-Baudry et al., 1997). Signals were prewhitened and then convolved by a family of complex Morlet's wavelets $w(t, f)$, one for each frequency, as a function of time:

$$w(t, f) = A e^{-t^2/2\sigma_t^2} e^{2i\pi f t}$$

With $\sigma_f = 1/2\pi\sigma_t$. The coefficient A was set at:

$$(\sigma_t \sqrt{\pi})^{-1/2}$$

in order to normalize the wavelets such that their total energy was equal to 1. The family of wavelets was characterized by a constant ratio f/σ_f, which was set to 5. Slow and

fast gamma power estimates were then z-scored across the entire recording session and averaged across respective frequency ranges and across tetrodes with place cell recordings. The maximum value of the resulting time-varying power was used to obtain a single slow gamma value and a single fast gamma value for each theta cycle.

Phase-phase coupling (Figure S5).

Phase–phase coupling plots were constructed based on the methods presented in a previous paper (Belluscio et al., 2012). Theta phase-slow gamma phase coupling was calculated as a bivariate histogram of the instantaneous theta and slow gamma phases (see "Phase analyses" section of Experimental Procedures) across significant slow gamma sequences (Figure S5A). Shuffled data were generated for comparison purposes, and shuffling procedures were based on those used previously (Belluscio et al., 2012). In each slow gamma sequence, slow gamma phases were randomly shifted between 1 and 100 ms, whereas theta phases remained the same. A 2-D histogram for shuffled data was then generated using the shifted slow gamma phases and non-shifted theta phases, and this procedure was repeated 1000 times. The final shuffled theta phase–slow gamma phase coupling plot was constructed by averaging all of the histograms from shuffled data (Figure S5B). The same procedure was performed for theta-fast gamma phase-phase coupling, except that instantaneous theta and fast gamma phases from significant fast gamma sequences were used (Figure S5C-D).

n:m phase-phase locking (Figure S5E)

In order to estimate how many gamma cycles occurred in a theta cycle, the n:m phase-locking ratio was calculated between theta and slow gamma, and between theta and fast gamma (Belluscio et al., 2012; Tass et al., 1998). We measured the mean resultant length (R value) of the distribution of phase differences:

$$\Delta\mathrm{phase}_{n:m}(t) = n \times \mathrm{phase}_{\mathrm{theta}}(t) - m \times \mathrm{phase}_{\mathrm{gamma}}(t)$$

on each theta sequence for different n:m ratios (i.e., *1:1, 1:2, …,1:12*). $R = 1$ represents a perfect unimodal distribution of n:m phase differences (Rayleigh test for uniformity), whereas $R = 0$ indicates that the n:m phase difference comes from a uniform distribution. The R value curves plotted for theta-slow gamma phase-phase coupling and theta-fast gamma phase-phase coupling were averaged across all significant slow gamma sequences and all significant fast gamma sequences, respectively (Figure S5E).

Alternative method for creating mock gamma cycles (Figure S5L)

For each slow and fast gamma sequence, slow and fast gamma phases were estimated within gamma cycles as described in the "Phase analyses" section of the Experimental Procedures. Then, for each slow and fast gamma sequence, wholly intact gamma cycles (i.e., those cycles occurring entirely within the slow or fast gamma sequence) were identified and randomly shuffled within their associated sequence. Partial gamma cycles occurring at the ends of the sequence were swapped within their associated sequence. This method provided a way to create mock gamma cycles without requiring arbitrary assignment of gamma phases to time points (i.e., the actual estimated gamma phases were maintained within each mock gamma cycle). Spike times were not

shuffled such that the original theta phases associated with spike times were preserved. Thus, gamma phases were shuffled relative to spike times, but the sequence of theta phases associated with spike times remained intact. This procedure was repeated 1000 times for each slow and fast gamma sequence.

Cross-correlation of gamma peaks (Figure S6B)

For LFP recordings from the whole session, slow and fast gamma peaks were identified as time points corresponding to slow and fast gamma phases of ~180° (see "Phase analyses" section of the Experimental Procedures) and exhibiting peak power exceeding 2 SD above the mean slow and fast gamma power, respectively. Numbers of slow gamma peaks and fast gamma peaks were separately counted within 100 ms sliding time bins, shifted by 10 ms. The resulting time series were then used to calculate cross-correlations between time-varying slow gamma and fast gamma peak counts.

Place cell spike rates during slow and fast gamma sequences (Figure S6C-E).

For each cell, spike rates were calculated within slow gamma sequences and fast gamma sequences for each recoding day. Cells were considered 'high firing' or 'low firing' for each gamma type if their spike rate was higher or lower, respectively, than the median spike rate from all cells for that particular gamma type.

Histology (Figure S1).

For verification of tetrode locations, brains were cut coronally into 30 μm sections and stained with cresyl violet. All tetrode tracks were identified, and the deepest location of each tetrode was determined by comparison across adjacent sections.

SUPPLEMENTAL REFERENCES

Battaglia, F.P., Sutherland, G.R., and McNaughton, B.L. (2004). Local sensory cues and place cell directionality: additional evidence of prospective coding in the hippocampus. J Neurosci *24*, 4541-4550.

Fox, S.E., and Ranck, J.B., Jr. (1981). Electrophysiological characteristics of hippocampal complex-spike cells and theta cells. Exp Brain Res *41*, 399-410.

Frank, L.M., Brown, E.N., and Wilson, M.A. (2001). A comparison of the firing properties of putative excitatory and inhibitory neurons from CA1 and the entorhinal cortex. J Neurophysiol *86*, 2029-2040.

Harris, K.D., Henze, D.A., Csicsvari, J., Hirase, H., and Buzsaki, G. (2000). Accuracy of tetrode spike separation as determined by simultaneous intracellular and extracellular measurements. J Neurophysiol *84*, 401-414.

Henze, D.A., Borhegyi, Z., Csicsvari, J., Mamiya, A., Harris, K.D., and Buzsaki, G. (2000). Intracellular features predicted by extracellular recordings in the hippocampus in vivo. J Neurophysiol *84*, 390-400.

Tallon-Baudry, C., Bertrand, O., Delpuech, C., and Permier, J. (1997). Oscillatory gamma-band (30-70 Hz) activity induced by a visual search task in humans. J Neurosci *17*, 722-734.

Tass, P., Rosenblum, M.G., Weule, J., Kurths, J., Pikovsky, A., Volkmann, J., Schnitzler, A., and Freund, H.J. (1998). Detection of n : m phase locking from noisy data: Application to magnetoencephalography. Phys Rev Lett *81*, 3291-3294.